Potential Chronological Disturbance of the D'Orbigny Angrite Inferred from Discordant 26 Al Ages

Cécile Deligny, Maxime Piralla, Johan Villeneuve, Evelyn Füri, Yves Marrocchi

The Astrophysical Journal Letters, 975:L16 (14pp), 2024 November 1 https://doi.org/10.3847/2041-8213/ad8654

Potential Chronological Disturbance of the D'Orbigny Angrite Inferred from Discordant ^{26}Al Ages

Cécile Deligny[1,2], Maxime Piralla[1,3], Johan Villeneuve[1], Evelyn Füri[1], and Yves Marrocchi[1]
[1] Université de Lorraine, CNRS, CRPG, UMR 7358, 54000 Nancy, France; cecile.deligny@nrm.se
[2] Department of Geosciences, Swedish Museum of Natural History, SE-104 05 Stockholm, Sweden
[3] Max Planck Institute for Solar System Research, Justus-von-Liebig-Weg 3, 37077 Göttingen, Germany
Received 2024 July 16; revised 2024 October 04; accepted 2024 October 13; published 2024 October 29

Abstract

Angrites originate from the early-formed differentiated angrite parent body. The pristine volcanic angrite D'Orbigny is devoid of brecciation, shock effects, or any evidence of secondary processes and is thus key for studying the early stages of planetary accretion and differentiation. However, chronometers used to establish the formation chronology of angrites (including D'Orbigny) yield discordant ages, either (i) suggesting that secondary processes could have disturbed the apparent formation ages or (ii) being taken as evidence of heterogeneous distribution of ^{26}Al in the early solar system. Yet spinel is minimally susceptible to secondary parent body processes and therefore a reliable target for establishing precise ^{26}Al–^{26}Mg ages. Here, we present the first in situ ^{26}Al–^{26}Mg analyses of spinel and plagioclase in D'Orbigny. Individual mineral assemblages provide distinct ages: olivine–spinel shows a well-defined isochron with an initial Al ratio ($[^{26}Al/^{27}Al]_i$) of $(5.39 \pm 0.85) \times 10^{-6}$, indicating formation at 2.35 $^{+0.25}_{-0.22}$ Myr after the formation of calcium–aluminum-rich inclusions (CAIs), whereas plagioclase–olivine defines an isochron with $[^{26}Al/^{27}Al]_i = (7.46 \pm 1.87) \times 10^{-7}$, implying formation at 4.40 $^{+0.44}_{-0.38}$ Myr after CAIs, consistent with previous MC-ICP-MS studies. This temporal gap can be attributed to secondary processes such as metamorphic or impact-generated diffusion. Thus, D'Orbigny and other angrites do not represent an immaculate anchor for chronometric comparison. This complexity should be considered in future studies, especially when using D'Orbigny as an anchor to discuss the chronology of the early solar system.

Unified Astronomy Thesaurus concepts: Cosmochronology (332); Achondrites (15); Isotopic abundances (867); Meteorites (1038)

1. Introduction

Angrites originated from a differentiated planetesimal (the angrite parent body, APB; K. Keil 2012 and references therein; F. L. Tissot et al. 2022) thought to have formed early in the solar system history, around ~0.4–1.5 Myr after the condensation of calcium–aluminum-rich inclusions (CAIs; T. Kleine et al. 2012; M. Schiller et al. 2015). Angrites thus provide fundamental insights into the early stages of planetary accretion and differentiation. In detail, angrites are mafic to ultramafic rocks that are divided into volcanic and plutonic groups according to their cooling history (D. W. Mittlefehldt & M. M. Lindstrom 1990; D. W. Mittlefehldt et al. 1998, 2002). Volcanic angrites are assumed to have cooled rapidly (T. Mikouchi et al. 2001; D. W. Mittlefehldt et al. 2001, 2002), implying that distinct radiometric systems should give, within errors, concordant formation ages (M. H. Dodson 1973). In addition, most volcanic angrites are (i) unbrecciated and unshocked and (ii) have been relatively preserved from secondary parent-body and terrestrial alteration processes (G. A. Brennecka & M. Wadhwa 2012; K. Keil 2012 and references therein). Therefore, volcanic angrites are key for cross-calibrating relative ages derived from short-lived dating techniques with absolute ages determined using long-lived radionuclides (e.g., F. L.-H Tissot et al. 2017).

Of the volcanic angrites, D'Orbigny is the most extensively studied due to the large amount of material available (16.55 kg), its unbrecciated and unshocked features, and the absence of any direct evidence of secondary alteration, despite having been found in a farm field and left there for almost two decades (G. Kurat et al. 2001; D. W. Mittlefehldt et al. 2002; C. Floss et al. 2003; K. Keil 2012 and references therein; M. E. Sanborn & M. Wadhwa 2021). Consequently, various in situ and bulk isotopic radiochronometric analyses have been performed on D'Orbigny (Figure 1), including absolute U–Pb and U-corrected Pb–Pb chronometry (Y. Amelin 2008; G. A. Brennecka & M. Wadhwa 2012; F. L.-H Tissot et al. 2017) and relative ^{26}Al–^{26}Mg (J. Baker et al. 2005; L. Spivak-Birndorf et al. 2009; M. Schiller et al. 2010, 2015), ^{53}Mn–^{53}Cr (L. E. Nyquist et al. 2003; D. P. Glavin et al. 2004; N. Sugiura et al. 2005; Q.-Z. Yin et al. 2009; S. J. McKibbin et al. 2013), ^{182}Hf–^{182}W (A. Markowski et al. 2007; T. Kleine et al. 2012), ^{147,146}Sm–^{143,142}Nd , and ^{176}Lu–^{176}Hf systems (A. Bouvier et al. 2015; M. E. Sanborn et al. 2015). D'Orbigny is also considered as an anchor for certain radiometric systems for which the initial ratios estimated for CAIs are not known with sufficient precision (e.g., S. J. Desch et al. 2023b), such as ^{53}Mn–^{53}Cr (anchored to Pb–Pb; K. Zhu et al. 2019).

Nonetheless, the absolute Pb–Pb and relative ^{26}Al–^{26}Mg and ^{182}Hf–^{182}W ages of D'Orbigny disagree when anchored to CAIs ($t_{CAIs} = 4567.30 \pm 0.16$ Ma; Y. Amelin et al. 2010; J. N. Connelly et al. 2012; Figure 1, Table S1). Although there is no consensus on the origin of this discrepancy, several possibilities have been put forth. On one hand, CAIs and the APB may have formed from reservoirs with different initial ^{26}Al abundances (e.g., M. Schiller et al. 2015; K. K. Larsen et al. 2016). On the other hand, recent studies challenged the

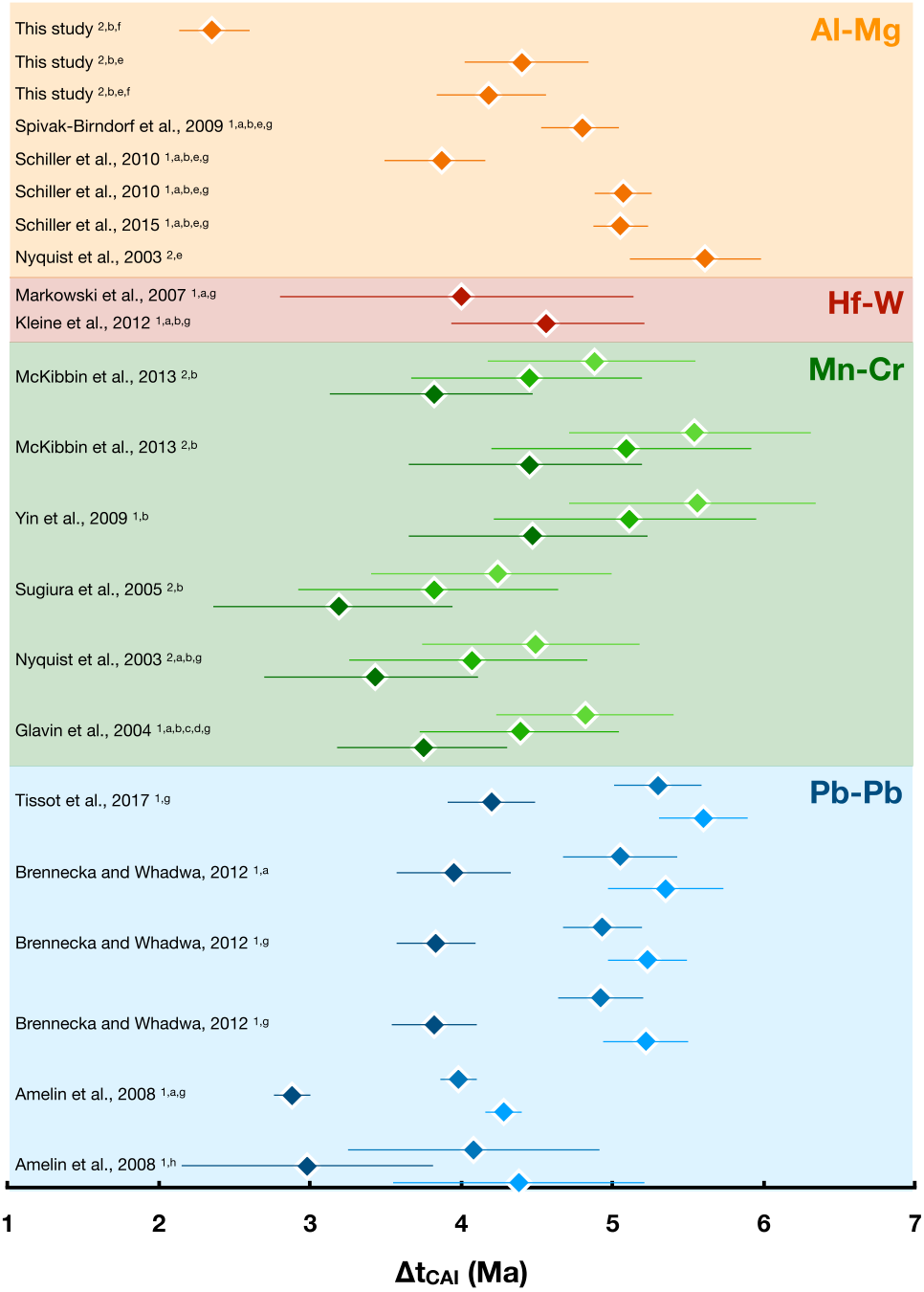

Figure 1. Formation ages of D'Orbigny obtained by bulk and in situ analyses of different geochronometers. ^{26}Al–^{26}Mg ages are reported in orange using a half-life of 0.717 Myr and $(^{26}Al/^{27}Al)_i = (5.23 \pm 0.13) \times 10^{-5}$ (B. Jacobsen et al. 2008). ^{182}Hf–^{182}W ages are reported in red with a half-life of 8.9 Myr and $(^{182}Hf/^{180}Hf)_i = (1.018 \pm 0.043) \times 10^{-4}$ (T. S. Kruijer et al. 2014). ^{53}Mn–^{53}Cr ages are reported in light green or green using a half-life of 3.7 Myr and $(^{53}Mn/^{55}Mn)_i = (6.54 \pm 0.44) \times 10^{-6}$, matching the CAIs age of Y. Amelin et al. (2010) and J. N. Connelly et al. (2012), or $(^{53}Mn/^{55}Mn)_i = 7.37 \pm 0.60 \times 10^{-6}$, matching the CAIs age of A. Bouvier et al. (2011), respectively. Dark green data points are reported using a half-life of 3.8 Myr and $(^{53}Mn/^{55}Mn)_i = (8.09 \pm 0.65) \times 10^{-6}$ (S. J. Desch et al. 2023b). Pb–Pb ages are reported in shades of blue relative to different CAI formation ages of 4568.7 Ma (light blue; M. Piralla et al. 2023), 4568.36 ± 0.20 Ma (blue; S. J. Desch et al. 2023a, 2023b), and 4567.30 ± 0.16 Ma (dark blue; Y. Amelin et al. 2010; J. N. Connelly et al. 2012). Superscripts indicate analyses and phases used to obtain ages: 1, bulk analyses; 2, in situ analyses; a, pyroxene; b, olivine; c, glass; d, chromite; e, plagioclase; f, spinel; g, bulk; h, concordia. Data sets are summarized in Table S1.

notion that the age of the solar system can be defined by the absolute Pb–Pb age of CAIs, instead proposing older ages of 4568.7 ± 0.7 (M. Piralla et al. 2023) or 4568.36 ± 0.20 Ma (S. J. Desch et al. 2023a, 2023b). Interestingly, these reevaluated CAI condensation ages provide a chronology that is consistent for both chondrules and achondrites (M. Piralla et al. 2023; S. J. Desch et al. 2023b).

The underlying assumption that all chronometers should give the same relative ages for volcanic angrites is also debatable. Sm–Nd and Lu–Hf chronometers record disturbed mineral ages in several angrites, including D'Orbigny. This indicates that thermal diffusion, likely induced by multiple impact events, affected the APB (A. Bouvier et al. 2015; M. E. Sanborn et al. 2015). Conversely, such events are not

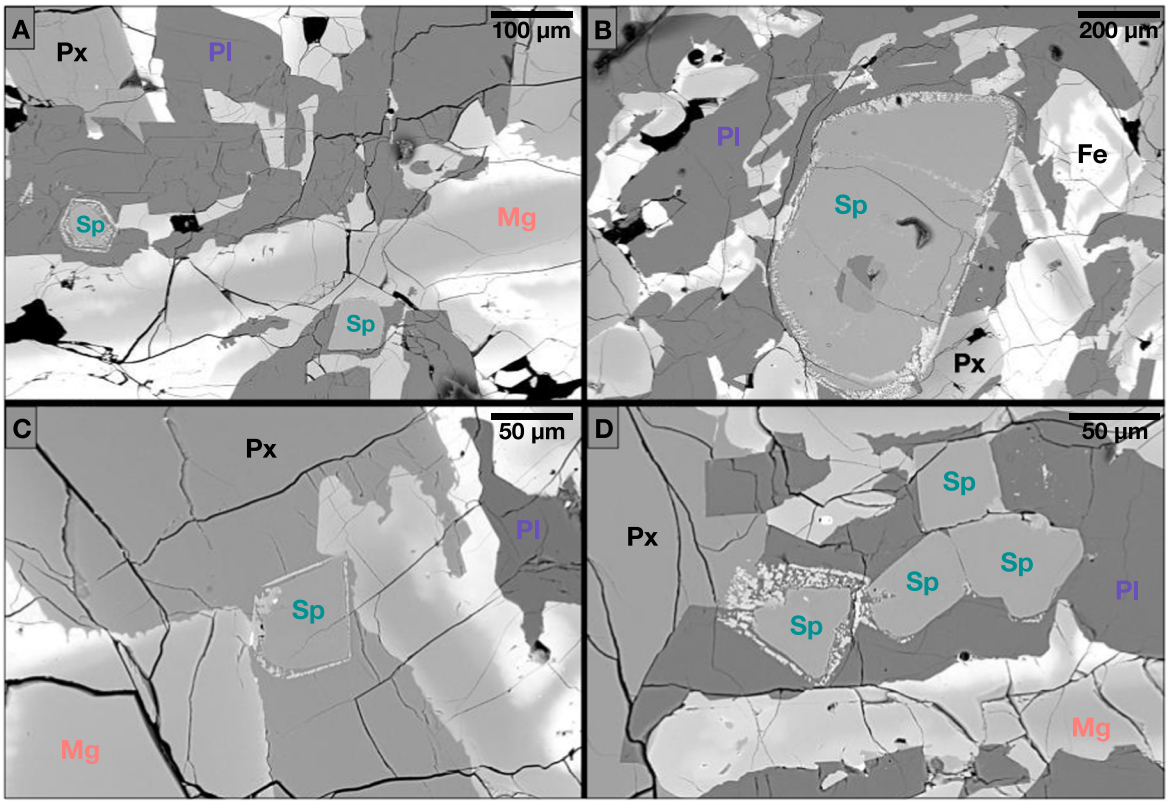

Figure 2. BSE images of D'Orbigny. (A, B) Plagioclase, Mg- and Fe-rich olivine, pyroxene, and spinel grains from the dense part of the meteorite (section N1170). One unusually large spinel with plagioclase and pyroxene inclusions was observed in this thin section (B). (C, D) Plagioclase, Fe-rich olivine, pyroxene, and spinel grains from the porous part of the meteorite (section N1179). Mg, Mg-rich olivine; Fe, Fe-rich olivine; Pl, plagioclase; Px, pyroxene; Sp, spinel. Most spinel grains in D'Orbigny have a thin Cr-rich rim, but SIMS analyses were only performed in the middles of spinel grains.

recorded by Pb–Pb, ^{26}Al–^{26}Mg, ^{53}Mn–^{53}Cr, and ^{182}Hf–^{182}W systematics in angrites, perhaps due to the distinct diffusion rates of the different elements in minerals used for radioactive dating (D. J. Cherniak 2001; J. Ganguly & M. Tirone 1999, 2001; J. Ganguly et al. 2007), preferentially resetting fast-diffusing elements compared to slow-diffusing ones (M. E. Sanborn et al. 2015). In addition, the textural and O isotopic characteristics of three volcanic angrites have recently been interpreted as evidence for impact events and mixing between the impactor(s) and the APB (A. J.-V. Riches et al. 2012; C. Deligny et al. 2021; B. G. Rider-Stokes et al. 2023a, 2023b). Despite the absence of any measurable O isotopic contamination from such an impactor, D'Orbigny is texturally and chemically similar to those angrites and may therefore have been affected by impact-related processes (B. G. Rider-Stokes et al. 2023a).

Recently, Mg-spinel grains in chondrites were shown to be robust targets for establishing precise ^{26}Al–^{26}Mg ages because they are less affected by secondary asteroidal processes compared to other mineral phases (e.g., plagioclase) and mesostasis (M. Piralla et al. 2023). Mg-spinel grains can thus be used to estimate the formation age of D'Orbigny and, by inference, the degree of secondary alteration of the APB. Here, we used this new methodology to obtain the first in situ ^{26}Al–^{26}Mg data for different mineral phases in D'Orbigny. Based on our results, we discuss the potential perturbation of the different radiochronometers and the larger use of D'Orbigny as a cosmochronological anchor.

2. Material and Methods

2.1. Samples

We surveyed three sections of D'Orbigny (N1, N1170, N1179). N1 was purchased from a reputable meteorite dealer and prepared at the Centre de Recherches Pétrographiques et Géochimiques (CRPG; Nancy, France; see C. Deligny et al. 2021 for sample preparation details). N1170 and N1179 are thin and thick sections, respectively, provided by the Naturhistorisches Museum Wien (Wien, Austria). N1 and N1170 are derived from the dense part of the meteorite, whereas N1179 samples the porous part (G. Kurat et al. 2001).

2.2. Scanning Electron Microscopy and Electron Probe Microanalyzer Analyses

Backscattered electron (BSE) images of the three sections were acquired by scanning electron microscopy (SEM; JEOL JSM-6510, CRPG) to identify olivine, plagioclase, and spinel grains (Figure 2). Their chemical compositions were determined using (i) a CAMECA SX-Five electron probe microanalyzer (EPMA) at CAMPARIS (Sorbonne University, Paris, France) and (ii) a JEOL JXA-8230 EPMA at CRPG (Nancy, France).

2.3. ^{26}Al–^{26}Mg Measurements

2.3.1. Analytical Conditions

We performed Mg and Al isotopic analyses of 41 spinel, 28 olivine, and 19 plagioclase grains by secondary ion mass

spectrometry (SIMS) using the CAMECA LG-SIMS 1280-HR2 at the CRPG, following the analytical protocol developed by J. Villeneuve et al. (2009), T.-H. Luu et al. (2013), and M. Piralla et al. (2023). O^- primary ions were emitted from a Hyperion-II radio frequency source focused into a 10–20 nA, $\leqslant 10\ \mu$m diameter beam rastered over $5 \times 5\ \mu m^2$. Transfer optics were tuned using a maximum area of 80 μm (100× magnification). $^{24}Mg^+$, $^{25}Mg^+$, $^{26}Mg^+$, and $^{27}Al^+$ secondary ions were measured in multicollection mode using four off-axis Faraday cups (FCs): L1, C, H1, and H'2 equipped with 10^{11}, 10^{12}, 10^{12}, and 10^{11} Ω resistors, respectively. The total counting time was 200 s after 90 s of presputtering rastered over $8 \times 8\ \mu m^2$. Exit slits were set on preset #1, corresponding to a nominal mass resolution ($m/\Delta m$) of 2500. Although this mass resolution is lower than that required to remove Mg hydride interferences, A. T. Hertwig et al. (2019) confirmed that interferences from $^{48}Ca^{2+}$ and hydrides ($^{24}MgH^+$) are negligible compared to the $^{24}Mg^+$ and $^{25}Mg^+$ signals. To further limit hydride interferences, a liquid N_2 trap was used to maintain the pressure at $<1 \times 10^{-8}$ mbar in the analysis chamber. All SIMS analytical spots were subsequently checked by SEM, and any spots located near fractures or not completely within a single phase were excluded from the data set (Figure C1). Isotopic compositions are reported in delta prime notation (δ'), using the logarithmic definition (E. D. Young & A. Galy 2004) and normalized to the values $[^{25}Mg/^{24}Mg]_{Ref} = 0.12663$ and $[^{26}Mg/^{24}Mg]_{Ref} = 0.13932$ (E. J. Catanzaro et al. 1966) as

$$\delta^{25,26}\text{Mg'} = 1000 \cdot \ln\left(\frac{(^{25,26}Mg/^{24}Mg)_{Sample}}{(^{25,26}Mg/^{24}Mg)_{Ref}}\right). \quad (1)$$

Typical internal errors on each measurement were estimated to be <0.05‰ for δ^{25}Mg' and δ^{26}Mg' for spinel and olivine grains and <0.5‰ for plagioclases.

2.3.2. Instrumental Mass Fractionation and ^{26}Mg Excess

Eight terrestrial or synthetic standards (San Carlos olivine, Ipanko 4 Mg-spinel, Miyake Jima anorthite, BHVO MORB, KL2-G glasses, JV1 diopside, gold, and Saint-Paul enstatite) were used to calibrate the instrumental mass fractionation of Mg isotopes during SIMS analyses (e.g., K. P. Jochum et al. 2005, 2006, 2011; G. Giuliani et al. 2017). Assuming that (i) natural fractionations in extraterrestrial samples are negligible compared to instrumental mass fractionation and (ii) their true Mg isotopic compositions are close to 0‰ (e.g., M. B. Olsen et al. 2016; H.-W. Chen et al. 2018; Z. Deng et al. 2021), we consider that the ^{26}Mg excess due to the radioactive decay of ^{26}Al, expressed as $\delta^{26}Mg^*$, can be obtained directly from the mass-independent composition Δ^{26}Mg' as follows:

$$\delta^{26}\text{Mg}^* \approx \Delta^{26}\text{Mg'} = \delta^{26}\text{Mg'} - \delta^{25}\text{Mg'}/\beta, \quad (2)$$

where β is the coefficient of the instrumental mass-fractionation power law. Typical β was 0.511 ± 0.005 (2 SD). Typical reproducibility of Δ^{26}Mg' was estimated to be (i) 0.1‰ (1 SD) and 0.01‰ (1 SE) for Ipanko 4 Mg-spinel and (ii) 0.06‰ (1 SD) and 0.01‰ (1 SE) for San Carlos olivine.

2.3.3. Al and Mg Ion Yields

Because Al and Mg have slightly different ion yields during SIMS analyses, their relative yields must be precisely determined and corrected by determining the relative sensitivity factor (RSF) before any $(^{26}Al/^{27}Al)_i$ ratios can be calculated from isochrons. RSF is expressed as

$$RSF_{Al/Mg} = \frac{(^{27}Al/^{24}Mg)_{measured}}{(^{27}Al/^{24}Mg)_{true}}, \quad (3)$$

with $^{27}Al/^{24}Mg$ determined from the elemental abundance of Al and Mg for each standard and the atomic abundance of Al and Mg. This gives for this analytical session an $RSF_{Al/Mg}$ of 0.72 ± 0.05 for olivine, 1.20 ± 0.02 for spinel, and 0.79 ± 0.04 for anorthite (2 SE).

2.3.4. Isochron Regression

Isochron regressions, as well as mass-dependent fractionation line and regressions, were computed using IsoplotR 4.2 (P. Vermeesch 2018) with the maximum probability options (i.e., Model 1; D. York et al. 2004).

2.4. Oxygen Isotopic Measurements

The oxygen isotopic compositions of spinels were measured by SIMS using the CAMECA LG-SIMS 1270-E7 at the CRPG (N. Bouden et al. 2021; G. L.-F Morin et al. 2022) using the same analytical conditions as Y. Marrocchi et al. (2024).

3. Results

D'Orbigny is mainly composed of long laths of anorthite (An > 99), skeletal to subhedral calcic olivine, and subhedral to euhedral Al–Ti-bearing calcic pyroxene (G. Kurat et al. 2001, 2004; D. W. Mittlefehldt et al. 2002; C. Floss et al. 2003; K. Keil 2012 and references therein). Accessory phases include Fe–Cr-bearing spinel, troilite, and ulvöspinel (e.g., D. W. Mittlefehldt et al. 2002). Anorthites display almost homogeneous chemical compositions, whereas pyroxenes are zoned and the rims of olivine grains are enriched in calcium (up to ∼21 wt.%; e.g., G. Kurat et al. 2001, 2004; D. W. Mittlefehldt et al. 2002; C. Floss et al. 2003). Spinels are ∼20–50 μm in diameter, except for one large spinel with a diameter of ∼600 μm (Figure 2(B)). Spinels are Al- and Fe-rich (51.2–55.7 wt.% Al_2O_3, 21.7–25.5 wt.% FeO, 11.8–13.5 wt.% MgO, 8.2–10.6 wt.% Cr_2O_3, and <0.19 wt.% SiO_2; Table S2). Plagioclases are Si- and Al-rich (43–44 wt.% SiO_2, 35 wt.% Al_2O_3, 20 wt.% CaO, and <1 wt.% FeO).

All spinels observed here were enclosed in plagioclase and pyroxene, except for one trapped in plagioclase–olivine intergrowths in section N1. Because olivine and plagioclase were the first minerals to form during crystallization, followed by pyroxene with Fe and Al zoning (D. W. Mittlefehldt et al. 2002), spinel must have formed early.

The six spinels measured in the three sections of D'Orbigny have oxygen isotopic compositions plotting, within errors, on the terrestrial fractionation line (TFL; i.e., average $\Delta^{17}O = -0.17 \pm 0.24$‰; Table S3). They do not derive from CAIs but instead crystallized in situ during the evolution of the APB ($\Delta^{17}O_{APB} = -0.066 \pm 0.016$‰; B. G. Rider-Stokes et al. 2023a). Including all 88 ^{26}Al–^{26}Mg analyses in a single isochron gives an initial aluminum isotopic ratio $(^{26}Al/^{27}Al)_i$ of $(9.21 \pm 1.84) \times 10^{-7}$ (MSWD = 2.22; Table 1, S4). This isochron reflects a formation age for D'Orbigny of 4.18 $^{+0.38}_{-0.34}$ Myr after CAIs when using $(^{26}Al/^{27}Al)_i = 5.23 \times 10^{-5}$ for CAIs (B. Jacobsen et al. 2008) and a ^{26}Al half-life of 0.717 Myr (F. G. Kondev et al. 2021). However, each mineral assemblage yields a distinct age (Figures 1, 3, A1; Table 1). Olivine–spinel shows a well-defined isochron with

Table 1.
Initial Al Isotopic Ratios $(^{26}Al/^{27}Al)_i$ and Initial Mg Isotopic Ratios $(\mu^{26}Mg^*_0)$ of Mineral Isochrons for D'Orbigny and Corresponding Ages after CAIs Formation.

Isochrons Unit	$(^{26}Al/^{27}Al)_i$	2σ	$\mu^{26}Mg^*_0$ [b] (ppm)	2σ (ppm)	MSWD	Δt_{CAIs} (Myr)	−2σ (Myr)	+2σ (Myr)	n_{iso} [c]
Ol + Sp + Pl	9.21×10^{-7}	1.84×10^{-7}	66	13	2.22	4.18	−0.34	0.38	88
Sp + Ol	5.39×10^{-6}	8.47×10^{-7}	2	18	0.82	2.35	−0.22	0.25	69
Pl + Ol	7.46×10^{-7}	1.87×10^{-7}	3	18	0.60	4.40	−0.38	0.44	47
Pl + Ol (filtered)[a]	7.11×10^{-7}	2.24×10^{-7}	3	18	0.55	4.45	−0.42	0.51	45

Notes.
[a] Filtered: rejected samples are indicated in Table S4 and by data points with black contours in Figure 3.
[b] $\mu^{26}Mg^*_0$ is defined as the intercept of the isochron, similarly to $\delta^{26}Mg^*_0$, but express in part per million (ppm) instead of part-per-thousand (‰).
[c] n_{iso} indicates the number of analyses included in the isochron.

$(^{26}Al/^{27}Al)_i = (5.39 \pm 0.847) \times 10^{-6}$ (MSWD = 0.82, $n = 69$; Figures 1, 3, A1; Table 1, S4), corresponding to $\Delta t_{CAIs} = 2.35\ ^{+0.25}_{-0.22}$ Myr. Plagioclase–olivine defines a distinct isochron with $(^{26}Al/^{27}Al)_i = (7.46 \pm 1.87) \times 10^{-7}$ (MSWD = 0.60, $n = 47$; Figures 1, 3, A1; Table 1, S4), significantly lower than spinel assemblages and corresponding to $\Delta t_{CAIs} = 4.40\ ^{+0.44}_{-0.38}$ Myr.

4. Discussion

Although angrites generally lack evidence for widespread shock metamorphism (D. W. Mittlefehldt et al. 1998), some samples display features that may result from thermal metamorphism such as (i) homogeneous compositions of clinopyroxene crystals, (ii) petrographic textures analogous to metamorphic textures in terrestrial rocks (S. M. Kuehner et al. 2006), and (iii) perturbed Sm–Nd and Lu–Hf systematics (A. Bouvier et al. 2015; M. E. Sanborn et al. 2015). The absence of any such evidence of thermal metamorphism in D'Orbigny (D. W. Mittlefehldt et al. 2002) implies that its pristine isotopic signatures have been preserved. Accordingly, D'Orbigny is generally considered to represent an archetypal example of a pristine and unprocessed volcanic angrite and is thus suitable for anchoring relative dating systems (e.g., ^{53}Mn–^{53}Cr) onto the absolute Pb–Pb timeline (e.g., G. A. Brennecka & M. Wadhwa 2012; F. L.-H Tissot et al. 2017).

However, our ^{26}Al–^{26}Mg results show that olivine–spinel and olivine–plagioclase assemblages in D'Orbigny record different formation ages of $2.35\ ^{+0.25}_{-0.22}$ and $4.40\ ^{+0.44}_{-0.38}$ Myr after CAIs, respectively (Figures 1, 3, A1), with each MSWD being lower and more consistent with a proper isochron compared to the olivine–spinel–plagioclase isochron (respectively, 0.82 and 0.60 compared to 2.22). This apparent temporal gap can either (i) reflect an analytical artifact during SIMS analyses or (ii) result from secondary alteration processes within the APB. The former appears unlikely because the $^{27}Al/^{24}Mg$ ratios estimated from EPMA and SIMS measurements are consistent (Figures 4, A2–A4), implying that our correction of Al and Mg yields via the RSF was accurate. Furthermore, the formation ages of plagioclase grains estimated by bulk and in situ methods are concordant (Figures 1, C2; L. Spivak-Birndorf et al. 2009; M. Schiller et al. 2010, 2015); the difference between the formation ages of spinel and plagioclase grains is therefore presumably the result of secondary processes (e.g., impacts, magmatic intrusions).

Metamorphism- or impact-generated diffusion can totally or partially reset radiochronometers depending on the elements and minerals considered. Regarding ^{26}Al–^{26}Mg systematics, Mg self-diffusion is notably faster in plagioclase than in Mg-spinel (Y. J. Sheng et al. 1992; H.-P. Liermann & J. Ganguli 2002; A. M. Suzuki et al. 2008; J. A. Van Orman et al. 2014; K. Vogt et al. 2015). This implies that secondary processes should have a very limited effect on ^{26}Al–^{26}Mg ages derived from olivine–spinel assemblages in D'Orbigny (Y. J. Sheng et al. 1992; M. Piralla et al. 2023). Indeed, the homogeneous chemical compositions of spinels in D'Orbigny preclude later episodes of Mg diffusion or Fe–Mg interdiffusion in spinel grains (Figure 2, Table S2). Our data thus demonstrate that the crystallization age of D'Orbigny is ∼2 Myr older than previously estimated (Figure 1).

The temporal gap between the formation ages estimated using olivine–spinel and olivine–plagioclase assemblages could result from partial resetting, presumably by thermal events such as impacts and/or melt intrusion on the APB. We note, however, that Mg diffusion characteristics in spinel and anorthite are not markedly different as Mg diffusion in plagioclase depends on An# (Y. J. Sheng et al. 1992; A. M. Suzuki et al. 2008; J. A. Van Orman et al. 2014; K. Vogt et al. 2015). Similar secondary isotopic disturbances have also been reported for Sm–Nd and Lu–Hf radiochronometers in angrites and eucrites (A. Bouvier et al. 2015, M. E. Sanborn et al. 2015). Furthermore, chemical zonings in olivine (i.e., Ca-rich rims) and pyroxene may reflect the local influx of a primitive melt during the initial crystallization of D'Orbigny (D. W. Mittlefehldt et al. 2002), which could have reset the initial Mg compositions of plagioclases. Although our results do not allow us to discriminate between impacts and melt intrusions, such events are required to explain the age gap between plagioclase and spinel grains in D'Orbigny. Finally, model ages can also be used for determining the age of the angrites—a single-step model, i.e., the age for which the $\delta^{26}Mg^*$ of a solar Al/Mg reservoir is equivalent to the $\delta^{26}Mg^*_i$ of the isochron, or a two-step model, i.e., the age of the Al–Mg differentiation so that $\delta^{26}Mg^*$ of a solar Al/Mg reservoir followed by the Al/Mg of the differentiated reservoir is equivalent to the $\delta^{26}Mg^*_i$ of the isochron. Such model ages, irrespective of being a single- or two-step models (depending on whether the $\delta^{26}Mg^*_i$ is higher than current solar $\delta^{26}Mg^*_i$) are mostly older than the ages determined from the $(^{26}Al/^{27}Al)_i$ ratio given by the isochron (A. Bouvier et al. 2011; M. Schiller et al. 2010, 2015). Such features are not only observed in angrites but also in other achondrites such as the eucrite Asuka 881394, whose two-step-formation $^{26}Mg^*$ model age of $\sim 2.15\ ^{+0.22}_{-0.18}$ Myr after CAIs does not match its ^{26}Al–^{26}Mg age of $3.69\ ^{+1.28}_{-1.27}$ Myr after CAIs (J. Wimpenny et al. 2019).

Recent independent studies have argued that a need exists to redefine the absolute age of CAI condensation to 4568.36 Myr (M. Piralla et al. 2023; S. J. Desch et al. 2023a, 2023b). This is based on the key assumption that the particularly pristine

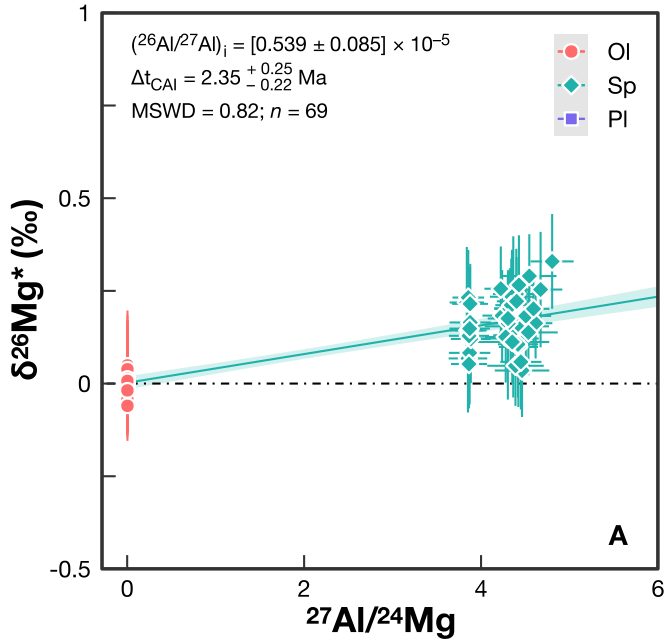

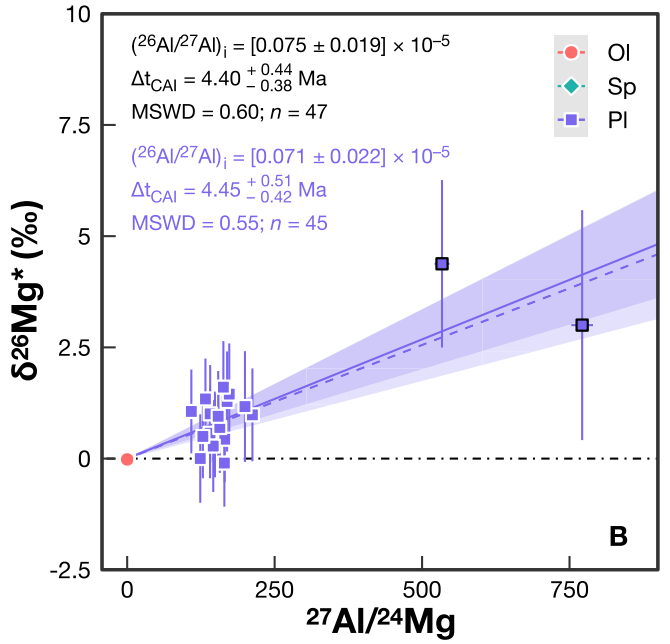

Figure 3. ^{26}Al–^{26}Mg isochrons for D'Orbigny based on (A) olivine and spinel grains and (B) olivine and plagioclase grains. Each mineral pair seems to define its own isochron, resulting in distinct ages. Solid lines and black text include all data, whereas the dashed line and colored text in (B) exclude the two outliers marked by black symbol borders. Errors are 2 SE.

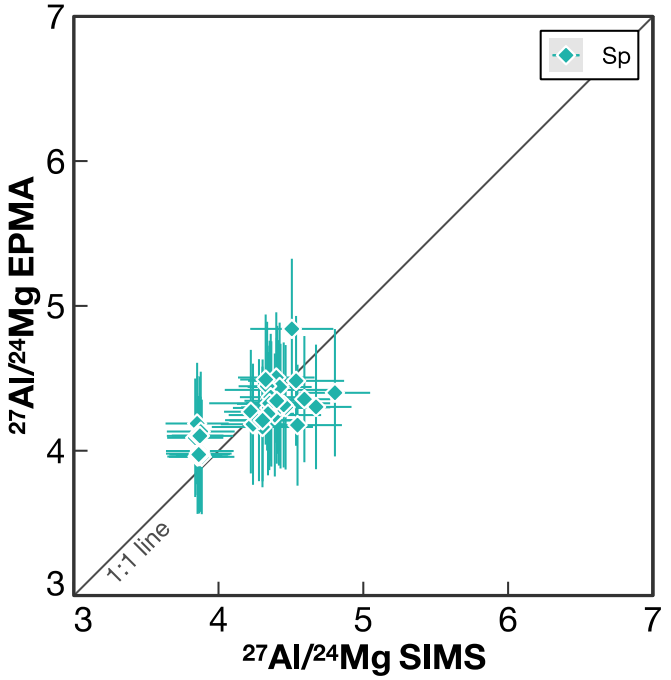

Figure 4. $^{27}Al/^{24}Mg$ ratios determined by EPMA compared to those determined by SIMS for analyzed spinels in D'Orbigny. The good agreement between the EPMA and SIMS values suggests that the appropriate RSF correction was applied when determining $^{27}Al/^{24}Mg$ by SIMS. The group of lower values correspond to larger spinel grains (Figure 2(B)). Errors are 2 SE. The r^2 value of 0.10 is low due to the small extent in the *x*-axis range; thus, spinel grains define rather a cluster of points than a good linear regression. They are however in good agreement with a 1:1 line, as shown by the root mean squared deviation of 0.18 and the mean absolute deviation of 0.14.

volcanic angrite D'Orbigny (and other volcanic angrites and/or achondrites) would yield similar relative ages for each radiochronometer (i.e., that $\Delta t_{CAIs,\ Pb\text{–}Pb} \approx \Delta t_{CAIs,\ Al\text{–}Mg} \approx \Delta t_{CAIs,\ Mn\text{–}Cr} \approx \Delta t_{CAIs,\ Hf\text{–}W}$). However, the most radiogenic phase, which generally most constrains the isochron, is not the same depending on the chronometer considered: for example, achondrite isochrons are mainly based on plagioclases/feldspars for ^{26}Al–^{26}Mg (L. Spivak-Birndorf et al. 2009; M. Schiller et al. 2010, 2015) and olivine for ^{53}Mn–^{53}Cr (D. P. Glavin et al. 2004; N. Sugiura et al. 2005) but mainly depend on pyroxenes and/or sequential leaching for Pb–Pb (Y. Amelin 2008). Our results demonstrate that the ^{26}Al–^{26}Mg systematics of D'Orbigny have been affected by some secondary event(s), resulting in different isotopic perturbations in each mineral phase. This implies that the signification of any "age" derived from an isochron must be carefully assessed, as a data set can either correspond to a true isochron (reflecting the age of formation in the absence of isotopic reset or the age of complete isotopic reset) or a disturbed isochron (in cases of partial isotopic reset). Therefore, D'Orbigny (and probably other angrites/achondrites) cannot be considered as an immaculate anchor for chronometric comparison. This complexity should be considered in future studies, especially those using D'Orbigny as an anchor for reassessing the CAI condensation age (M. Piralla et al. 2023; S. J. Desch et al. 2023a, 2023b; B. G. Rider-Stokes et al. 2023b).

Although our findings have implications on the chronology of the solar system and the potential heterogeneity of ^{26}Al, a definitive interpretation remains challenging due to its dependence on assumptions. First, we emphasize once again that, if alteration processes occurred on the APB, this significantly limits the information we can gather about (i) the initial ^{26}Al distribution in the disk and (ii) the early solar system chronology. Second, assuming that only plagioclase was affected by secondary alteration and that Al–Mg spinel and Pb–Pb ages are concordant, this would either imply (i) a heterogeneous distribution of ^{26}Al in the disk or (ii) a younger initial absolute age of the solar system of

about 4565.86 ± 0.33 Myr (Figure C2). The former interpretation would lead to a supracanonical $^{26}Al/^{27}Al_0$ of $[2.10 \pm 0.68] \times 10^{-4}$ or $[5.86 \pm 1.88] \times 10^{-4}$ assuming the age of CAIs to be 4567.30 Myr (J. N. Connelly et al. 2012) or 4568.36 Ma (M. Piralla et al. 2023; S. J. Desch et al. 2023b), respectively. Although supracanonical ratios have been reported in CAIs (E. D. Young et al. 2005), they do not reach such extreme values and have been discarded by later measurements (B. Jacobsen et al. 2008). The latter is also difficult to reconcile with the recent reevaluation of the initial age of the solar system settled at 4568.36 Myr (M. Piralla et al. 2023; S. J. Desch et al. 2023b). Third, it has been proposed that the $^{27}Al/^{24}Mg$ ~2 of basaltic meteorites cannot be directly produced from chondritic material with the $^{27}Al/^{24}Mg$ ~0.1 ratio (M. Schiller et al. 2010). This could either reflect partial melting of chondritic material, directly producing high $^{27}Al/^{24}Mg$ ratio magmas, or extensive planetesimal melting followed by magmatic differentiation, which could account for the high $^{27}Al/^{24}Mg$ ratios observed in volcanic angrites. In such scenarios, spinels may correspond to an early magmatic episode on the APB parent body, as suggested by their apparent older ^{26}Al ages. Consequently, they should not be included in an isochron with minerals that crystallized during the final magmatic episode that produced the quenched volcanic angrites. This would imply that both ^{26}Al ages inferred from spinel and plagioclase grains reflect distinct magmatic events, likely corresponding to an early fractionation episode and the final crystallization event forming the volcanic angrites, respectively. Notably, since the spinel ^{26}Al age is older than the two-step model age, this supports models of magmatic differentiation following large-scale planetesimal melting (M. Schiller et al. 2010). If correct, spinel and plagioclase data would decipher the magmatic history of the APB without challenging the current chronology, which has recently been reaffirmed based on a comprehensive compilation of chronological data (S. J. Desch et al. 2023b). Nevertheless, a direct comparison of different chronometers should approach cautiously, as they may record perturbation events differently. It is therefore essential to establish a comprehensive data set for each chronometer to better understand how secondary processes affect them.

Acknowledgments

We thank Ludovic Ferrière (Naturhistorisches Museum Wien) for providing two sections of D'Orbigny and Robert Dennen (RD Editing Services) for stylistic and linguistic corrections. We thank François Tissot and one anonymous reviewer for the helpful comments and Dieter Hartmann for the very efficient editorial handling. This work was supported by l'Agence Nationale de la Recherche (ANR) through grant CASSYSS ANR-18-CE31-0010-01 (PI: Johan Villeneuve), by INSU-PNP grant to J.V., by OTELo grant to J.V., and by the European Research Council (ERC) under the European Union's Horizon 2020 research and innovation program (grant agreement no. 715028 to E.F.). This is CRPG contribution #2857.

Data Availability

Original data from this study are available on the ORDaR repository: https://ordar.otelo.univ-lorraine.fr/record?id=10.24396/ORDAR-149

Appendix A
SEM Observations and EPMA Measurements

Quantitative analyses of major (Si, Al, Ca, Na, Mg, Fe) and minor (Ti, Mn, Cr, K, Ni, P) element concentrations in spinels and plagioclases were performed in two analytical sessions using an accelerating voltage of 15 kV and a probe current of 40 nA during the Paris session and 20 kV and 10 nA, respectively, during the Nancy session. A suite of natural reference materials was used for calibration and monitoring instrumental stability: olivine for Mg and Si, K-feldspar for K and Al, iron oxide for Fe, albite for Na, diopside for Ca, manganese titanite for Mn and Ti, chromite for Cr, Ni oxide for Ni, and apatite for P. On-peak and background counting times were 40 s for all elements for the Paris session. For the Nancy session, the total peak and background counting time was 200 s for Al, Ti, Ca, Mn, P, and Cr and 20 s for K, Na, Mg, Fe, and Si. Detection limits were 0.025 wt.% (Mg), 0.025 wt.% (Fe), 0.05 wt.% (Si), 0.005 wt.% (Ca), 0.02 wt.% (Al), 0.005 wt.% (Ti), 0.015 wt.% (Cr, P, K, Na), and 0.008 wt.% (Mn). The quality of all analyses was carefully assessed, and results with totals below 98% or above 102% were discarded (Table S2). Of note, no specific age difference was observed between analyses with totals <98% and those with totals of 98%–102% (Figures A1–A4).

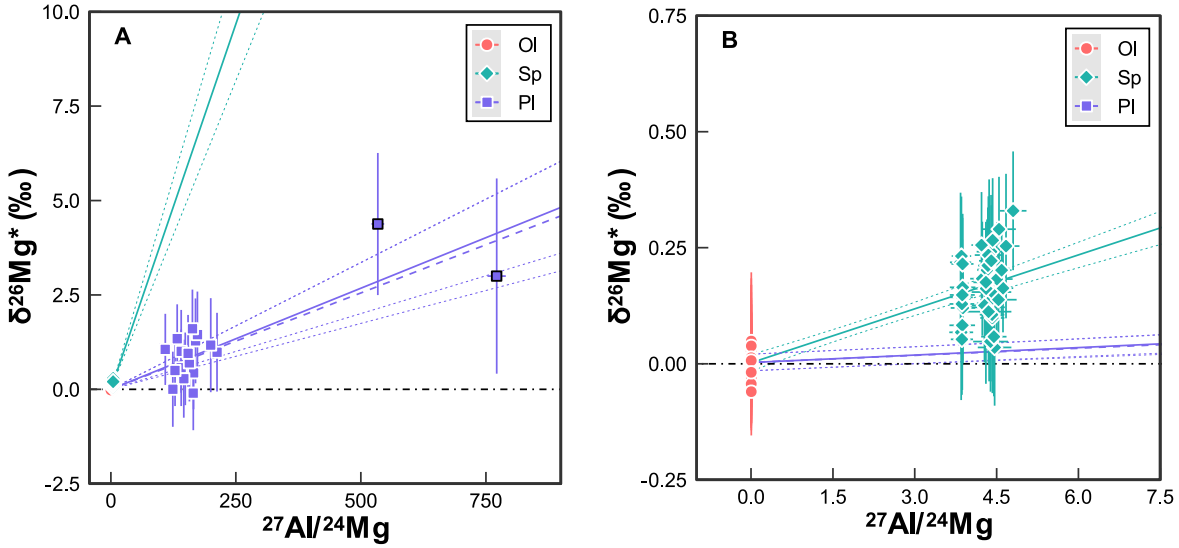

Figure A1. Isochrons for olivine–spinel and olivine–plagioclase assemblages similar to Figure 3 but with both isochrons overlaid. (A) Full view. The isochron inferred from olivine–spinel assemblages (turquoise) have a steeper slope than that inferred from olivine–plagioclase assemblages (purple), indicating that spinel records an older age than plagioclase. As shown in Figure 3 from the main text, variability over each isochron is quite small, as indicated by the low MSWDs for both isochrons. (B) Enlarged view to highlight the spinel data. Here, the spinel grains (turquoise) clearly exhibit a higher $\delta^{26}Mg^{*}$ value compared to the isochron from olivine–plagioclase assemblages (purple).

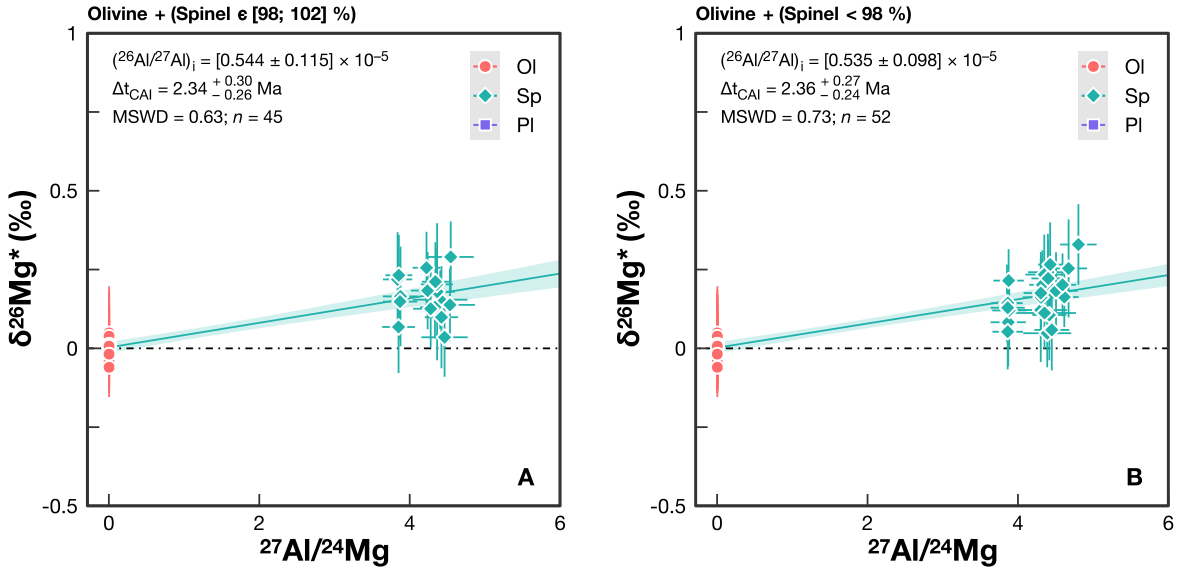

Figure A2. Isochrons for olivine–spinel assemblages for spinel with (A) EPMA totals between 98% and 102% and (B) EPMA totals <98%. Both isotopic and elemental ratios are from SIMS data. Note that EMPA data seem to be independent of SIMS quality as both isochrons gave the same results and $^{27}Al/^{24}Mg$ is consistent. The EPMA beam interaction with the sample is also different from that of the SIMS beam, and there might be a slight offset between the two, especially when EPMA was performed after SIMS measurements.

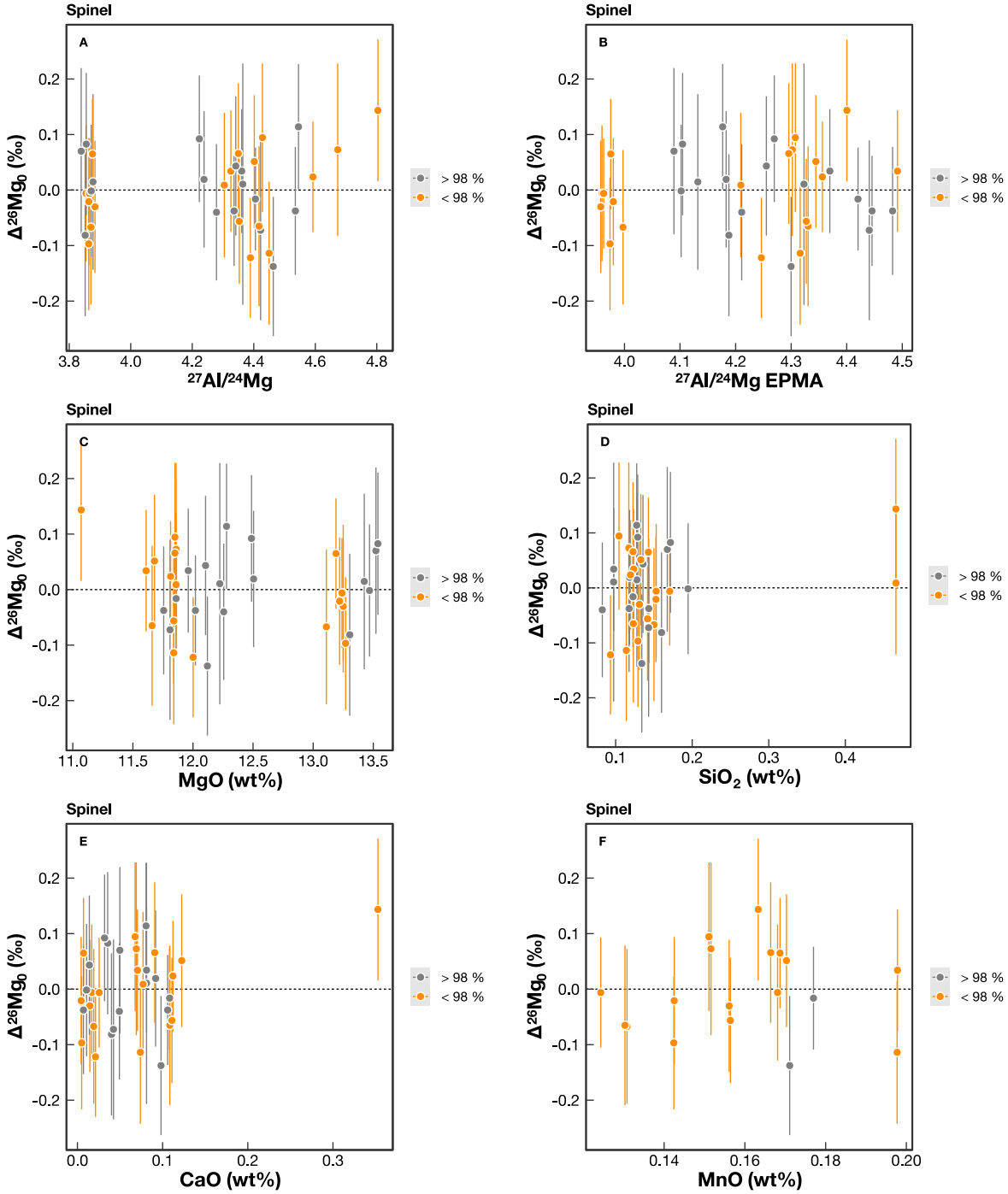

Figure A3. $\Delta^{26}Mg'_0$ as a function of elemental composition. $\Delta^{26}Mg'_0$ is defined as the $\Delta^{26}Mg'$ value at $^{27}Al/^{24}Mg = 0$ using the slope of the isochron for olivine–spinel assemblages, i.e., $(^{26}Al/^{27}Al)_i = 5.39 \times 10^{-6}$. It is expressed as $\Delta^{26}Mg'_0 = \Delta^{26}Mg' - (^{26}Al/^{27}Al)_i \times {}^{27}Al/^{24}Mg$. This allows a direct comparison of $\Delta^{26}Mg'$ values, even in the case of distinct $^{27}Al/^{24}Mg$ ratios. No significant $\Delta^{26}Mg'_0$ variation is observed across the range of compositions for each element. Note that $\Delta^{26}Mg'_0$ is distinct from $\delta^{26}Mg'^*_i$ to avoid confusion with the intercept of a proper isochron. Indeed, here, $\Delta^{26}Mg' = \delta^{26}Mg'^*$ because mass-independent fractionation is due to ^{26}Al decay.

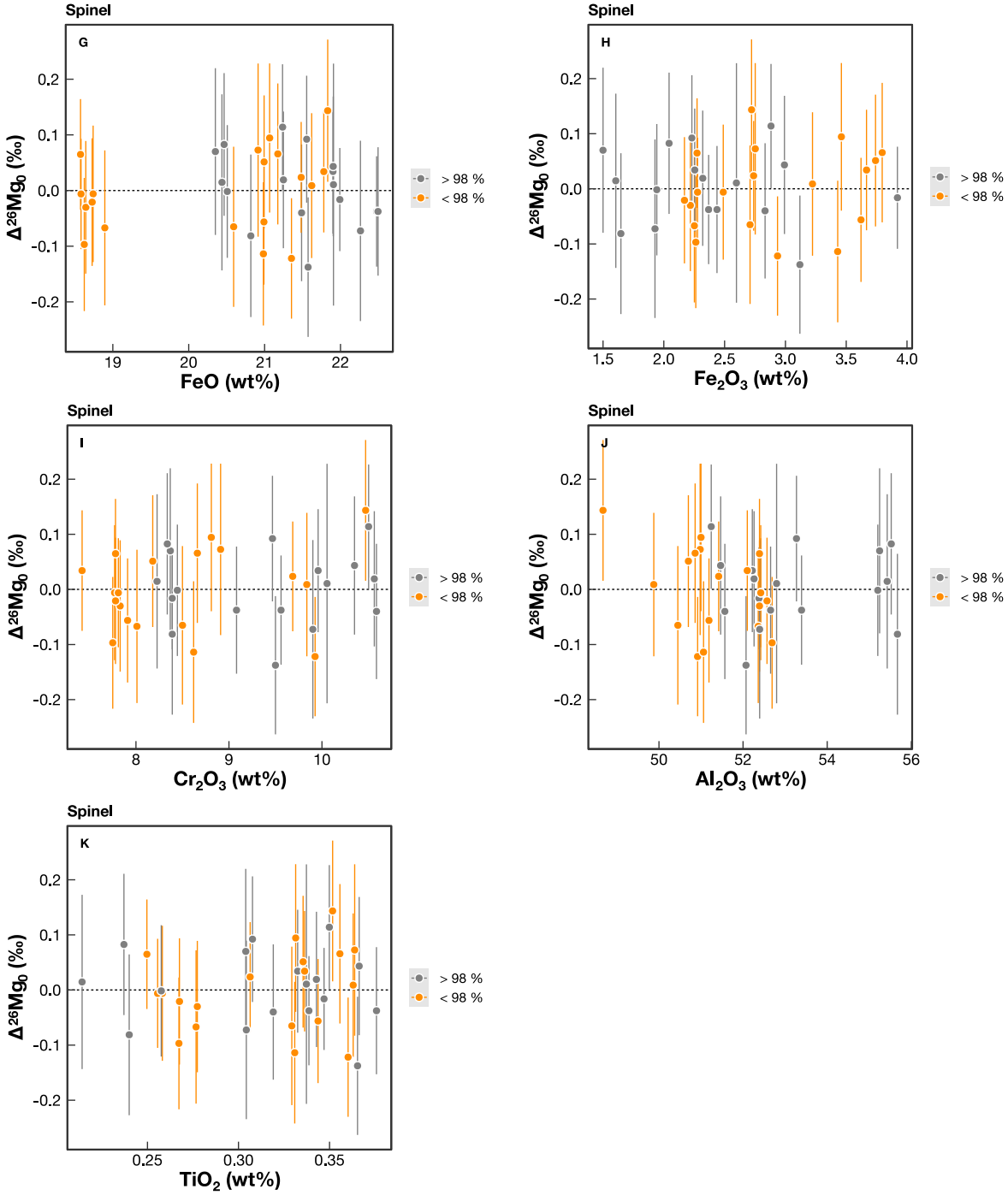

Figure A3. (Continued.)

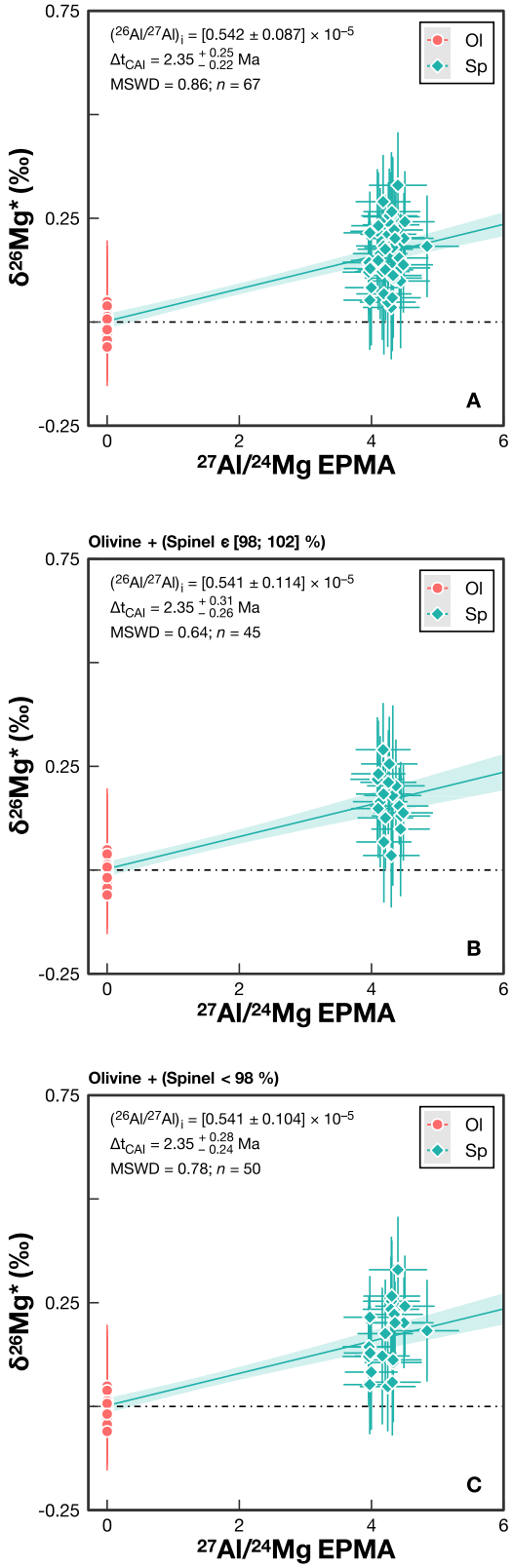

Figure A4. Isochrons using $^{27}Al/^{24}Mg$ ratios inferred from EPMA analyses (A) using all data available for spinel grains, (B) using only EPMA data with totals of 98%–102%, and (C) using only EPMA data with totals <98%. Panels (B) and (C) can be compared to panels (A) and (B) in Figure A2, respectively, which show SIMS data for $^{27}Al/^{24}Mg$. No difference is apparent between the two subsets, and the age determined here is similar to the SIMS-derived age from Figures 3, A2. This demonstrates that the RSF correction was performed correctly, and thus the $^{27}Al/^{24}Mg$ determined by SIMS are accurate (see also Figure 4).

Appendix B
Oxygen Isotopic Measurements

Oxygen isotopic compositions were measured SIMS using CAMECA LG-SIMS 1270-E7 at the CRPG (N. Bouden et al. 2021; Y. Marrocchi et al. 2024). $^{16}O^-$, $^{17}O^-$, and $^{18}O^-$ ions produced by a Cs^+ primary ion beam (~4 μm, 500 pA) were measured in multicollection mode using two off-axis FCs for $^{16,18}O^-$ and the axial electron multiplier (EM) for $^{17}O^-$. To remove $^{16}OH^-$ interference on the $^{17}O^-$ peak and achieve maximum flatness atop the $^{16}O^-$ and $^{18}O^-$ peaks, the entrance and exit slits of the central EM were adjusted to achieve a mass resolving power (MRP = $m/\Delta m$) of ~6000 for $^{17}O^-$. The OH contribution was negligible (<0.1%), and the ^{16}OH interference was well resolved. The multicollection FCs were set on exit slit 1 (MRP = 2500). The total measurement duration was 260 s, comprising 60 s of presputtering and 200 s of measurement. Four terrestrial standard materials (San Carlos olivine, Ipanko spinel, Rockport fayalite, and UWCr-3 chromite) were used to define the instrumental mass fractionation line for the three oxygen isotopes. We corrected the Cr-bearing spinel using the UWCr-3 chromite (P. R. Heck et al. 2010). To monitor any instrumental drift and to achieve good precision, the San Carlos olivine was reanalyzed after every 10 sample analyses. Oxygen isotopic compositions are expressed in δ notation as $\delta^{17,18}O = ([^{17,18}O/^{16}O]_{sample}/[^{17,18}O/^{16}O]_{V\text{-}SMOW} - 1) \times 1000‰$, where V-SMOW refers to Vienna Standard Mean Ocean Water. Samples related by mass-dependent fractionation to the V-SMOW composition plot along a line with a slope of 0.52, defining the TFL, whereas mass-independent variations are described by $\Delta^{17}O = \delta^{17}O - 0.52 \times \delta^{18}O$, representing vertical deviations from the TFL in a triple oxygen isotope diagram. Typical 2σ uncertainties, accounting for internal errors on each measurement and the external reproducibility of the standard, were estimated to be ~1‰ for $\delta^{18}O$, ~0.8‰ for $\delta^{17}O$, and ~1‰ for $\Delta^{17}O$. The error on $\Delta^{17}O$ was calculated by quadratically summing the errors on $\delta^{17}O$ and $\delta^{18}O$.

Appendix C
^{26}Al–^{26}Mg Measurements

Backscattered electron images of D'Orbigny spinels, after the Al and Mg isotopic measurements, are presented in Figure C1.

The backgrounds of the four FCs were determined during each analytical session. Background correction was done considering the true background value as the average of the backgrounds measured before and after the measurement. The correction was made following the formula of T.-H. Luu et al. (2013):

$$\delta^{x}Mg_{bkgcorr}' = \delta^{x}Mg_{raw}' + \Delta b_x/n_x \times 1000 - \Delta b_{24}/n_{24} \times 1000, \quad (C1)$$

with $x = 26$ or 25, n_x and n_{24} the count rates (in cps) for the ^{25,26}Mg and ^{24}Mg isotopes, and Δb_x and Δb_{24} the drifts (in cps) estimated for their background variations (Δb_i = measured background–extrapolated background).

Instrumental mass fractionation was monitored by repeated and interspersed analyses of terrestrial rock standards (San Carlos olivine, Ipanko 4 Mg-spinel, Miyake Jima anorthite, BHVO MORB, KL2-G glasses, JV1 diopside, gold, and Saint-Paul enstatite) prior to, during, and after the analytical sessions, ensuring that instrumental mass fractionation satisfies the relationship: $\alpha_{inst}25/24 = (\alpha_{inst}26/24)^{\beta}$, with $\alpha_{inst}25,26/24 = (^{25,26}Mg/^{24}Mg)_{measured}/(^{25,26}Mg/^{24}Mg)_{true}$, and β an exponential factor. β can vary from 0.51 in the case of purely kinetic reactions to 0.52 at equilibrium, depending on the fractionation kinetics (e.g., A. M. Davis et al. 2015; N. Dauphas & E. A. Schauble 2016).

In situ Mg isotopic data are reported in linearized form relative to $[^{26}Mg/^{24}Mg]_{Ref} = 0.13932$ and $[^{25}Mg/^{24}Mg]_{Ref} = 0.12663$ (E. J. Catanzaro et al. 1966):

$$\delta^{x}Mg' = \ln([^{x}Mg/^{24}Mg]_{Sample}/[^{x}Mg/^{24}Mg]_{Ref}) \times 1000. \quad (C2)$$

The excess of ^{26}Mg is then calculated using

$$\delta^{26}Mg^* = \delta^{26}Mg' - \delta^{25}Mg'/\beta. \quad (C3)$$

β was determined daily as the slope of the linear regression in a $\delta^{26}Mg' = f(\delta^{25}Mg')$ plot. Assuming that (i) natural fractionations in extraterrestrial samples are negligible compared to instrumental mass fractionation and (ii) their true Mg isotopic compositions are close to 0‰ (See also H.-W. Chen et al. 2018; Z. Deng et al. 2021), we consider that $\delta^{26}Mg^*$ can directly be obtained from the deviation from the mass-dependent fractionation line (Equation S3; A. T. Hertwig et al. 2019; M. Piralla et al. 2023). Using this methodology, instrumental mass fractionation does not need to be corrected to determine the ^{26}Mg excess of a sample, which might translate into a negligible effect of the possible mismatch of the β value between natural and instrumental fractionation. Uncertainties were calculated as the quadratic sum of internal reproducibility (given from a single sample measurement) and the external reproducibility on standards (average deviation of the mass-dependent fractionation line).

In practice, the mass-dependent fractionation line is estimated by a linear regression in a $\delta^{26}Mg' = f(\delta^{25}Mg')$ plot for each standard session using IsoplotR online or the IsoplotR R package version 4.2 (P. Vermeesch 2018). As we did not correct for instrumental mass-dependent bias, the raw mass-dependent fractionation line can present an offset, and Equation S3 should be rewritten as

$$\delta^{26}Mg^* = \delta^{26}Mg' - (\delta^{25}Mg' - \text{intercept})/\beta, \quad (C4)$$

where the intercept is most likely due to a residual mismatch of the intercalibration coefficients of the FCs, even after performing the FCs cross calibration.

Isochron regressions, as well as the mass-dependent fractionation line and regressions, were computed using IsoplotR 4.2 (P. Vermeesch 2018) with the maximum probability options (i.e., Model 1; D. York et al. 2004). The resulting ^{26}Al–^{26}Mg age was calculated relative to the "canonical" $^{26}Al/^{27}Al$ ratio of CAIs ($[5.23 \pm 0.13] \times 10^{-5}$; B. Jacobsen et al. 2008) using a ^{26}Al half-life of 0.717 Ma (F. G. Kondev et al. 2021; NuDat 3.0, National Nuclear Data Center). This allowed to compare the initial $^{26}Al/^{27}Al$ ratios obtained from different phases in D'Orbigny with different radiochronometers (Figure C2).

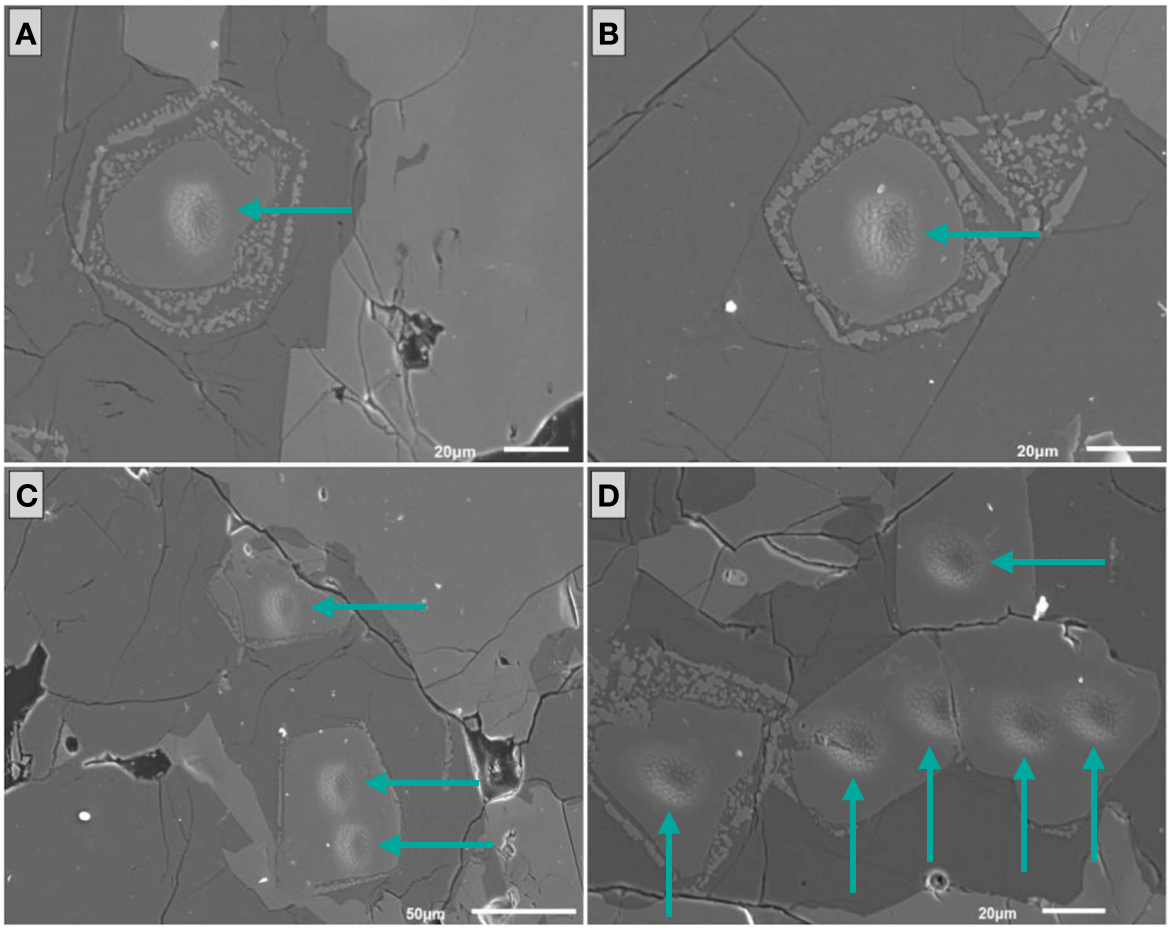

Figure C1. BSE images of spinel grains in D'Orbigny after SIMS analysis (SIMS craters indicated by the green arrows). (A–C) Section N1170 and (D) section N1179.

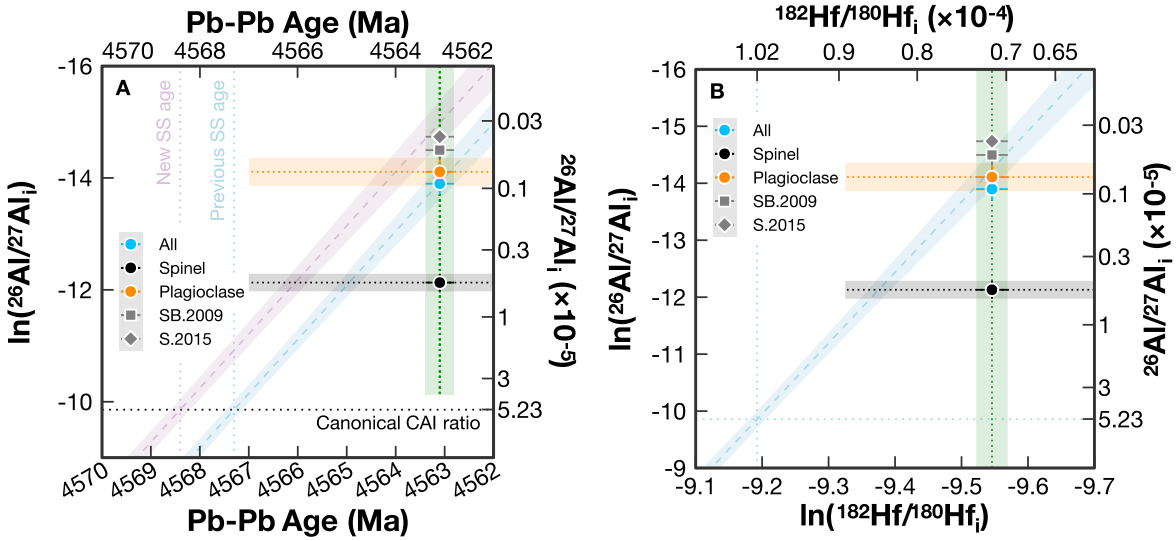

Figure C2. Comparison between different radiochronometers. (A) Initial $(^{26}Al/^{27}Al)_i$ (natural logarithm) vs. Pb–Pb ages of CAIs. (B) Initial $(^{26}Al/^{27}Al)_i$ (natural logarithm) vs. initial $(^{182}Hf/^{180}Hf)_i$ (natural logarithm). ^{26}Al–^{26}Mg systematics in spinel are clearly different from what is recorded by the Pb–Pb or Hf–W systems. This compromises our ability to anchor different chronometers and evaluate the start of the solar system and/or the homogeneity of short-lived radionuclides. Data derived from internal isochrons from this study use all data, only olivine–spinel assemblages, or only olivine–plagioclase assemblages. For comparison, data resulting from isochrons of L. Spivak-Birndorf et al. (2009; SB.2009) and M. Schiller et al. (2015; S.2015) include all olivine, pyroxene, plagioclase, and whole-rock analyses. Pb–Pb data are from the U-corrected Pb–Pb age of F. L.-H Tissot et al. (2017; from Y. Amelin 2008) and Hf–W data from T. Kleine et al. (2012). Horizontal dashed lines correspond to $\ln(^{26}Al/^{27}Al)_I$ for olivine–plagioclase and olivine–spinel from this study (orange and black), and the vertical dashed lines correspond to Pb–Pb age and $\ln(^{182}Hf/^{180}Hf)_i$ of D'Orbigny, respectively, for panel (A) and (B). Note that the points only make sense if the age recorded by both chronometers date the same event, especially when comparing chronometers based on distinct phases. See the text for more details.

ORCID iDs

Cécile Deligny https://orcid.org/0000-0002-9558-2677
Maxime Piralla https://orcid.org/0000-0001-9332-6250
Yves Marrocchi https://orcid.org/0000-0001-7075-3698

References

Amelin, Y. 2008, GeCoA, 72, 221
Amelin, Y., Kaltenbach, A., Iizuka, T., et al. 2010, E&PSL, 300, 343
Baker, J., Bizzarro, M., Wittig, N., Connelly, J., & Haack, H. 2005, Natur, 436, 1127
Bouden, N., Villeneuve, J., Marrocchi, Y., et al. 2021, FrEaS, 8, 601169
Bouvier, A., Blichert-Toft, J., Boyet, M., & Albarède, F. 2015, M&PS, 50, 1896
Bouvier, A., Brennecka, G. A., & Wadhwa, M. 2011, LPICo, 1639, 9054
Brennecka, G. A., & Wadhwa, M. 2012, PNAS, 109, 9299
Catanzaro, E. J., Murphy, T. J., Garner, E. L., & Shields, W. R. 1966, JRNBA, 70A, 453
Chen, H.-W., Claydon, J. L., Elliott, T., et al. 2018, GeCoA, 227, 19
Cherniak, D. J. 2001, ChGeo, 177, 381
Connelly, J. N., Bizzarro, M., Krot, A. N., et al. 2012, Sci, 338, 651
Dauphas, N., & Schauble, E. A. 2016, AREPS, 44, 709
Davis, A. M., Richter, F. M., Mendybaev, R. A., et al. 2015, GeCoA, 158, 245
Deligny, C., Füri, E., & Deloule, E. 2021, GeCoA, 313, 243
Deng, Z., Chaussidon, M., Ebel, D. S., et al. 2021, GeCoA, 299, 163
Desch, S. J., Dunlap, D. R., Dunham, E. T., Williams, C. D., & Mane, P. 2023a, Icar, 402, 115607
Desch, S. J., Dunlap, D. R., Williams, C. D., Mane, P., & Dunham, E. T. 2023b, Icar, 402, 115611
Dodson, M. H. 1973, CoMP, 40, 259
Floss, C., Crozaz, G., McKay, G., Mikouchi, T., & Killgore, M. 2003, GeCoA, 67, 4775
Ganguly, J., Ito, M., & Zhang, X. 2007, GeCoA, 71, 3915
Ganguly, J., & Tirone, M. 1999, E&PSL, 170, 131
Ganguly, J., & Tirone, M. 2001, M&PS, 36, 167
Giuliani, G., Fallick, A. E., Boyce, A. J., Pardieu, V., & Pham, V. L. 2017, CaMin, 55, 743
Glavin, D. P., Kubny, A., Jagoutz, E., & Lugmair, G. W. 2004, M&PS, 39, 693
Heck, P. R., Ushikubo, T., Schmitz, B., et al. 2010, GeCoA, 74, 497
Hertwig, A. T., Kimura, M., Ushikubo, T., Defouilloy, C., & Kita, N. T. 2019, GeCoA, 253, 111
Jacobsen, B., Yin, Q., Moynier, F., et al. 2008, E&PSL, 272, 353
Jochum, K. P., Stoll, B., Herwig, K., et al. 2006, GGG, 7, Q02008
Jochum, K. P., Willbold, M., Raczek, I., Stoll, B., & Herwig, K. 2005, GGRes, 29, 285
Jochum, K. P., Wilson, S. A., Abouchami, W., et al. 2011, GGRes, 35, 193
Keil, K. 2012, ChEG, 72, 191
Kleine, T., Hans, U., Irving, A. J., & Bourdon, B. 2012, GeCoA, 84, 186
Kondev, F. G., Wang, M., Huang, W. J., Naimi, S., & Audi, G. 2021, ChPhC, 45, 030001
Kruijer, T. S., Kleine, T., Fischer-Gödde, M., Burkhardt, C., & Wieler, R. 2014, E&PSL, 403, 317
Kuehner, S. M., Irving, A. J., Bunch, T. E., et al. 2006, LPI, 37, 1344
Kurat, G., Varela, M. E., Brandstätter, F., Wäsch, E., & Nazarov, M. A. 2001, LPI, 32, 1737
Kurat, G., Varela, M. E., Brandstätter, F., et al. 2004, GeCoA, 68, 1901
Larsen, K. K., Schiller, M., & Bizzarro, M. 2016, GeCoA, 176, 295
Liermann, H-P., & Ganguly, J. 2002, GeCoA, 66, 2903
Luu, T-H., Chaussidon, M., Mishra, R. K., et al. 2013, JAAS, 28, 67
Markowski, A., Quitte, G., Kleine, T., et al. 2007, E&PSL, 262, 214
Marrocchi, Y., Longeau, A., Goupil, R. L., et al. 2024, GeCoA, 371, 52
McKibbin, S. J., Ireland, T. R., Amelin, Y., Holden, P., & Sugiura, N. 2013, GeCoA, 123, 181
Mikouchi, T., Miyamoto, M., McKay, G., & Le, L. 2001, M&PSA, 36, A134
Mittlefehldt, D. W., Killgore, M., & Lee, M. T. 2001, LPI, 32, 2057
Mittlefehldt, D. W., Killgore, M., & Lee, M. T. 2002, M&PS, 37, 345
Mittlefehldt, D. W., & Lindstrom, M. M. 1990, GeCoA, 54, 3209
Mittlefehldt, D. W., McCoy, T. J., Goodrich, C. A., & Kracher, A. 1998, in Planetary Materials, ed. J. J. Papike (Berlin: De Gruyter), 523
Morin, G. L.-F., Marrocchi, Y., Villeneuve, J., & Jacquet, E. 2022, GeCoA, 332, 203
Nyquist, L. E., Shih, C. Y., Wiesmann, H., & Mikouchi, T. 2003, LPI, 34, 1388
Olsen, M. B., Wielandt, D., Schiller, M., Van Kooten, E. M.-M. E., & Bizzarro, M. 2016, GeCoA, 191, 118
Piralla, M., Villeneuve, J., Schnuriger, N., Bekaert, D. V., & Marrocchi, Y. 2023, Icar, 394, 115427
Riches, A. J.-V., Day, J. M.-D., Walker, R. J., et al. 2012, E&PSL, 353, 208
Rider-Stokes, B. G., Greenwood, R. C., Anand, M., et al. 2023a, NatAs, 7, 836
Rider-Stokes, B. G., Pittarello, L., White, L. F., et al. 2023b, LPICo, 2806, 1610
Sanborn, M. E., Carlson, R. W., & Wadhwa, M. 2015, GeCoA, 171, 80
Sanborn, M. E., & Wadhwa, M. 2021, M&PS, 56, 482
Schiller, M., Baker, J. A., & Bizzarro, M. 2010, GeCoA, 74, 4844
Schiller, M., Connelly, J. N., Glad, A. C., Mikouchi, T., & Bizzarro, M. 2015, E&PSL, 420, 45
Sheng, Y. J., Wasserburg, G. J., & Hutcheon, I. D. 1992, GeCoA, 56, 2535
Spivak-Birndorf, L., Wadhwa, M., & Janney, P. 2009, GeCoA, 73, 5202
Sugiura, N., Miyazaki, A., & Yanai, K. 2005, EP&S, 57, e13
Suzuki, A. M., Yasuda, A., & Ozawa, K. 2008, PCM, 35, 433
Tissot, F. L., Collinet, M., Namur, et al. 2022, GeCoA, 338, 278
Tissot, F. L.-H., Dauphas, N., & Grove, T. L. 2017, GeCoA, 213, 593
Van Orman, J. A., Cherniak, D. J., & Kita, N. T. 2014, E&PSL, 385, 79
Vermeesch, P. 2018, GeoFr, 9, 1479
Villeneuve, J., Chaussidon, M., & Libourel, G. 2009, Sci, 325, 985
Vogt, K., Dohmen, R., & Chakraborty, S. 2015, AmMin, 100, 2112
Wimpenny, J., Sanborn, M. E., Koefoed, P., et al. 2019, GeCoA, 244, 478
Yin, Q-Z., Yamashita, K., Yamakawa, A., et al. 2009, LPI, 40, 2060
York, D., Evensen, N. M., Martínez, M. L., & De Basabe Delgado, J. 2004, AmJPh, 72, 367
Young, E. D., & Galy, A. 2004, RvMG, 55, 197
Young, E. D., Simon, J. I., Galy, A., et al. 2005, Sci, 308, 223
Zhu, K., Moynier, F., Wielandt, D., et al. 2019, ApJ, 877, L13